JACS
JOURNAL OF THE AMERICAN CHEMICAL SOCIETY

Article

pubs.acs.org/JACS

Conformational Dynamics of a Seven Transmembrane Helical Protein *Anabaena* Sensory Rhodopsin Probed by Solid-State NMR

Daryl B. Good,[†] Shenlin Wang,[†,∥] Meaghan E. Ward,[†,‡] Jochem Struppe,[§] Leonid S. Brown,[†,‡] Józef R. Lewandowski,[⊥] and Vladimir Ladizhansky*[,†,‡]

[†]Department of Physics and [‡]Biophysics Interdepartmental Group, University of Guelph, Guelph, Ontario, N1G 2W1 Canada

[§]Bruker Biospin Ltd., Billerica, Massachusetts 01821, United States

[⊥]Department of Chemistry, University of Warwick, Coventry CV4 7AL, United Kingdom

Supporting Information

ABSTRACT: The ability to detect and characterize molecular motions represents one of the unique strengths of nuclear magnetic resonance (NMR) spectroscopy. In this study, we report solid-state NMR site-specific measurements of the dipolar order parameters and ^{15}N rotating frame spin−lattice ($R_{1\rho}$) relaxation rates in a seven transmembrane helical protein *Anabaena* Sensory Rhodopsin reconstituted in lipids. The magnitudes of the observed order parameters indicate that both the well-defined transmembrane regions and the less structured intramembrane loops undergo restricted submicrosecond time scale motions. In contrast, the $R_{1\rho}$ rates, which were measured under fast magic angle spinning conditions, vary by an order of magnitude between the TM and exposed regions and suggest the presence of intermediate time scale motions. Using a simple model, which assumes a single exponential autocorrelation function, we estimated the time scales of dominant stochastic motions to be on the order of low tens of nanoseconds for most residues within the TM helices and tens to hundreds of nanoseconds for the extracellular B−C and F−G loops. These relatively slow time scales could be attributed to collective anisotropic motions. We used the 3D Gaussian axial fluctuations model to estimate amplitudes, directions, and time scales of overall motions for helices and the extracellular B−C and F−G loops. Within this model, the TM helices A,B,C,D,E,F undergo rigid body motions on a time scale of tens of nanoseconds, while the time scale for the seventh helix G approaches 100 ns. Similar time scales of roughly 100−200 ns are estimated for the B−C and F−G loops.

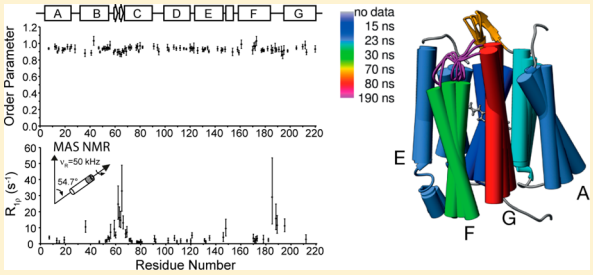

INTRODUCTION

Membrane proteins participate in the majority of life processes and perform numerous functions. Most extracellular stimuli experienced by the cell are first sensed by membrane receptors, which change their conformation and pass the signal to the inside of the cell. The ability of membrane proteins to undergo conformational changes implies a high intrinsic flexibility, which manifests in a complex hierarchy of internal motions, many of which are essential to protein function. Remarkably, this flexibility can be detrimental to the crystallization process and often needs to be suppressed for crystallographic studies,[1] which may result in a distorted view of functional dynamics.

Over the past decade, solid-state NMR (SSNMR) has been emerging as a powerful technique for studies of protein structure and dynamics. SSNMR is not limited by the requirement of solubility or crystallinity and, in principle, can be applied to molecules of arbitrary molecular weight. In particular, SSNMR has been successfully used for studies of membrane proteins in the physiologically relevant environment of a lipid bilayer.[2−7] Multidimensional magic angle spinning (MAS) SSNMR has also been used to site-specifically characterize dynamics in proteins. Cross-peak intensities in SSNMR spectra usually inversely correlate with the mobility of the corresponding residues and often serve as indicators of increased local mobility.[8−13] A more detailed view can be obtained from the analysis of motional narrowing of the line shapes of anisotropic interactions, such as chemical shift anisotropies and heteronuclear dipolar couplings,[8,14−18] which report on the amplitudes of local motions occurring on a time scale faster than the inverse of the probed interaction.

Nuclear spin relaxation times, T_1, T_2, and $T_{1\rho}$, and heteronuclear NOEs are commonly used in solution NMR for the detailed characterization of molecular motions in proteins.[19−21] Similarly, SSNMR has a long history of studies of protein dynamics.[22−26] In general, applications of these methods in SSNMR meet one principal complication: relaxation measurements in immobilized systems are dominated by coherent effects due to incompletely averaged dipolar interactions. Two approaches have recently been devised to remedy this problem. The first approach relies on the suppression of proton−proton interactions (and on the

Received: November 14, 2013
Published: January 27, 2014

   dx.doi.org/10.1021/ja411633w | J. Am. Chem. Soc. 2014, 136, 2833−2842

effective reduction of heteronuclear dipolar interactions under MAS) through the dilution of the proton bath by perdeuteration with back-exchange of the amide and other solvent-accessible sites.[27−30] Alternatively, relaxation measurements can be carried out under fast or ultrafast magic angle spinning, which was shown to suppress the coherent contributions to both the longitudinal and transverse relaxation rates. In particular, proton-driven spin diffusion (PDSD) contributions to the ^{15}N longitudinal relaxation rates become negligible at spinning rates above 20 kHz,[31,32] whereas much faster rates of 60 kHz or higher are needed to suppress the PDSD processes between carbonyl and aliphatic carbon atoms.[33] Likewise, fast MAS rates of >45 kHz, in combination with a spinlock, result in long ^{15}N $R_{1\rho}$ relaxation times dominated by stochastic contribution to the coherence lifetimes and directly report on motions on the nanosecond−microsecond time scale.[34]

Characterization of dynamics of membrane proteins[9,10,12,13,25,35−40] is more challenging than that of globular proteins in a microcrystalline state.[28−30,41−45] Detailed site-specific analyses of the time scales and amplitudes of motions in polytopic membrane proteins are sparse, owing to relatively low sensitivity of solid-state NMR spectra and to the fact that extensive resonance assignments are available for only a few of them. In this contribution, we use solid-state NMR to probe the conformational flexibility of *Anabaena* Sensory Rhodopsin (ASR), a recently discovered microbial photosensor from cyanobacterium *Anabaena* sp. PCC 7120.[46] ASR has the typical rhodopsin architecture of a seven transmembrane helical (7TM) bundle, with retinal bound to lysine 210 on the seventh helix (helix G) through the Schiff base.[47,48] ASR has a unique phototransduction cascade, started by the absorption of light by retinal, which subsequently isomerizes from all-*trans* to 13-*cis* conformation, causing structural rearrangements within the protein and modulating its binding affinity with the cognate soluble cytoplasmic transducer (ASRT).[47,49] Interactions between ASRT and DNA may, in turn, regulate the expression of several proteins responsible for photosynthesis and circadian clock in *Anabaena*,[50] thus providing a convenient mechanism for single protein color sensing.[47,51−53]

In previous studies, we have used solid-state NMR to obtain nearly complete spectroscopic assignments of ASR[48,54] and have determined its high-resolution structure.[7] Underscoring the effect of environment on the membrane protein conformation, ASR oligomerizes into stable trimers in both detergents and lipids[55] but exists in a dimeric state in crystals.[56] While seven helices form a similarly organized rigid transmembrane core in ASR in both crystals[56] and lipids,[7] its extramembranous loop regions are less structurally defined. Reduced NMR cross-peak intensities of the residues in the loops (discussed in the following) and elevated B-factors in the crystal structure[47] for residues at the protein−solvent interface point at their potential flexibility. These residues have exchangeable backbone amides,[7,48] which again points to a potentially higher degree of flexibility within the hydrogen/deuterium (H/D) exchangeable fragments. Chemical shift assignments have revealed the presence of double conformers for some of the residues on the cytoplasmic side,[54] indicating either static disorder, or a very slow exchange (longer than 500 ms), as revealed by the absence of exchange cross-peaks in the proton-driven spin diffusion ^{13}C−^{13}C correlation spectra collected with long mixing.[7] Additionally, as ASR interacts with a soluble transducer in a light-dependent manner, it is likely to undergo large conformational changes between the bound and unbound states in the course of its photocycle. Changes in the solvent-accessible surface of the protein detected using H/D exchange measurements under illumination specifically suggest the possibility of a substantial movement of the seventh helix G.[57]

In this study, we directly probe the conformational flexibility of ASR. We used solid-state NMR to site-specifically measure the backbone dipolar order parameters and the transverse spin−spin relaxation rates ($R_{1\rho}$). As ASR has a non-H/D-exchangeable hydrophobic core[48] similar to other polytopic membrane proteins,[58−60] the latter measurements were performed on fully protonated samples at fast MAS (50 kHz). Our data indicate that the transmembrane regions undergo motions on the time scale of tens of nanoseconds, while larger relaxation rates for the B−C and F−G loops correspond to slower motions on the tens to hundreds of nanoseconds time scale, overall suggesting the possibility of collective motions of both the TM domains and exposed regions.

EXPERIMENTAL SECTION

Sample Preparation. Three ASR samples were used in these studies. All dipolar chemical shift correlation spectroscopy (DIPSHIFT) experiments were conducted on two ASR samples with uniform ^{15}N labeling but alternate ^{13}C labeling, obtained from cells grown on glycerol labeled at positions 1 and 3 (1,3-ASR in the following) or at position 2 (2-ASR). Measurements of $R_{1\rho}$ were carried out on a uniformly ^{15}N,^{13}C-labeled ASR sample (UCN ASR).

Samples were prepared as described previously.[7,48] Briefly, C-terminally truncated histidine-tagged ASR was expressed in BL21 Codonplus RIL *Escherichia coli* grown on M9 minimal medium using 1 g of ^{15}N-labeled ammonium chloride as the sole nitrogen source and 4 g of either 2-^{13}C- or 1,3-^{13}C-labeled glycerol or $^{13}C_6$-labeled glucose as carbon sources for alternately or uniformly labeled samples, respectively. Retinal was added exogenously at the time of induction at a concentration of 7.5 μM.

The cells were collected by centrifugation and then treated with lysozyme and DNase I before being broken by sonication. The membrane fraction was solubilized in 1% DDM (*n*-dodecyl β-D-maltoside) at 4 °C. Liposomes were prepared by hydrating dried DMPC and DMPA mixed in 9:1 ratio (w/w). Liposomes were mixed with purified ASR solubilized in detergent, at a protein/lipid ratio of 2:1 (w/w). Biobeads were used for detergent removal. Proteoliposomes were collected by ultracentrifugation at 900 000*g* for 6 h. 1,3-ASR and 2-ASR were packed into thin wall 3.2 mm rotors for DIPSHIFT experiments, and the UCN ASR sample was packed into a 1.3 mm NMR rotor for $R_{1\rho}$ measurements.

NMR Spectroscopy. Dipolar order parameters for four couplings were measured using 3D dipolar chemical shift correlation experiments. Z-filtered TEDOR (ZF-TEDOR)[61,62] recoupling was employed for the measurement of ^{15}N−$^{13}C_\alpha$ and ^{15}N−^{13}C′ dipolar couplings, and transverse MREV (TMREV)[63] recoupling was used to probe the strengths of ^{15}N−^{1}H and $^{13}C_\alpha$−$^{1}H_\alpha$ interactions. Details of the pulse sequences are given in Figure S1 in the Supporting Information. All DIPSHIFT experiments were performed on a Bruker Avance III 600 MHz spectrometer, using a 3.2 mm triple-resonance (HCN) EFREE probe for ZF-TEDOR measurements or a 3.2 mm HCN TL2 probe for TMREV experiments. For the measurement of $^{13}C_\alpha$−$^{1}H_\alpha$ couplings, TMREV recoupling was combined with the 2D NCA spectroscopy for site-specific resolution, and the experiments were conducted on 1,3-ASR and 2-ASR samples. ^{15}N−^{1}H couplings were measured on both 1,3-ASR and 2-ASR samples using 2D NCA spectroscopy, with "afterglow" magnetization used to record complementary 2D NCO spectra.[64] Measurements of ^{15}N−$^{13}C_\alpha$ and ^{15}N−^{13}C′ couplings were conducted on the 1,3-ASR and 2-ASR samples, where we simultaneously recorded complementary NCA and

NCO spectra. The 84 kHz SPINAL-64 decoupling[65] was used during both the direct and indirect chemical shift evolution periods. Sample temperature was calibrated using external references of methanol[66] and KBr[67] and maintained at 280 K.

The TMREV DIPSHIFT experiments (Figure S1) were performed at a spinning frequency of 8 kHz. They used $^{1}H/^{15}N$ cross-polarization (CP)[68] of 2 ms duration with an ^{15}N field strength of 35 kHz with the proton field ramped 10% around the n = 2 Hartmann−Hahn (HH)[69] matching condition. $^{15}N/^{13}C_{\alpha}$ band-selective CP[70] was done using a 5 ms contact time with a 22 kHz spinlock field on ^{15}N and with the carbon field ramped linearly (10%) around the n = 1 HH condition. The $^{15}N/^{13}C'$ band-selective CP was done using the same parameters as for $^{15}N/^{13}C_{\alpha}$ except that the ^{13}C carrier frequency was placed at 175 ppm in the middle of the carbonyl spectral region. TMREV recoupling was implemented in a constant time manner as shown in Figure S1, with four TMREV elements per rotor cycle (TMREV-4),[63] which required proton radio frequency (RF) field strength of ∼96 kHz (90° pulse duration of 2.6 μs). The total echo period was set to 12 rotor cycles. TPPM decoupling[71] of 96 kHz was used during the remainder of the echo period.

ZF-TEDOR DIPSHIFT experiments were performed at a spinning frequency of 12 kHz, using an "out and back" detection scheme.[62] The initial $^{1}H/^{13}C$ CP was performed with a 2 ms contact time, with a ^{13}C RF field of 50 kHz and the proton field linearly ramped around the n = 1 HH condition (10% ramp). Polarization transfer between ^{13}C and ^{15}N was accomplished using the TEDOR method with REDOR pulse trains[72] implemented on the nitrogen channel with ^{15}N 180° pulses of 14 μs. TPPM proton decoupling[71] of 90 kHz was used during REDOR periods. ^{13}C 90 and 180° pulses were 4 and 8 μs, respectively. Z-filters of 167 μs duration (two rotor cycles) with a RF proton field of 12 kHz were used after both REDOR pulse trains to remove artifacts from the remaining homonuclear J-couplings between carbon spins.[62]

Measurements of ^{15}N transverse relaxation rate constants, $R_{1\rho}$, were performed on a Bruker 800 MHz Avance III spectrometer using a 1.3 mm ultrafast MAS Bruker probe tuned to ^{1}H, ^{13}C, and ^{15}N at a spinning rate of 50 kHz and using recycle delays of 600 ms. The sample temperature was kept at 280 K. $^{1}H/^{15}N$ cross-polarization was performed with a contact time of 2 ms, a 30 kHz RF field on ^{15}N, and a 10% ramp around 80 kHz on ^{1}H. $^{15}N/^{13}C_{\alpha}$ band-selective CP was implemented with a 5 ms contact time matching the n = 1 double-quantum HH matching condition using a RF field of 20 kHz on nitrogen and a 10% ramped RF field centered at 30 kHz on ^{13}C. No proton decoupling was used during $^{15}N/^{13}C_{\alpha}$ CP. The ^{15}N transverse magnetization decay was probed at ^{15}N spinlock fields of 10, 12, 14, and 16 kHz. For each of the field strengths, five points were taken for 0, 20, 50, 100, and 200 ms durations of the spinlock. Spinlock power was calibrated at 50 kHz using rotary resonance recoupling by following the ^{15}N signal intensity as a function of lock field.[73,74] TPPM48[75] low-power decoupling was used during both direct and indirect acquisition with a proton RF field optimized around 12 kHz.

Data Analysis. Carbon chemical shifts were indirectly referenced to 2,2-dimethyl-2-silapentane-5-sulfonic acid (DSS) by adjusting the position of the ^{13}C adamantane downfield peak to 40.48 ppm,[76] and nitrogen chemical shifts were referenced indirectly. TMREV and ZF-TEDOR spectra were processed using NMRPipe.[77] Peak amplitudes were extracted using CARA software[78] based on previously reported assignments (Figure 1, BMRB entry 18595).[54] The amplitudes of isolated peaks were taken without modification, while partially overlapped peaks were fit to Gaussian line shapes, and linear deconvolutions were performed for neighboring peaks to estimate their amplitudes.

The dipolar order parameters were determined as ratios $\langle S \rangle = D_{expt}/D_{rigid}$ between the experimentally determined dipolar couplings, D_{expt}, and the rigid limit, D_{rigid}. Peak amplitudes extracted from the TMREV experiments were fit using the theory outlined by Hohwy, Griffin, and co-workers,[63] which is summarized in the Supporting Information. To account for the effects of weakly coupled protons, a distant proton was included in the simulation, following previously described procedures.[63,79] Fit parameters were overall amplitude, relaxation time, and the one-bond $^{1}H-^{15}N$ or $^{1}H-^{13}C$ dipolar couplings. The rigid limit

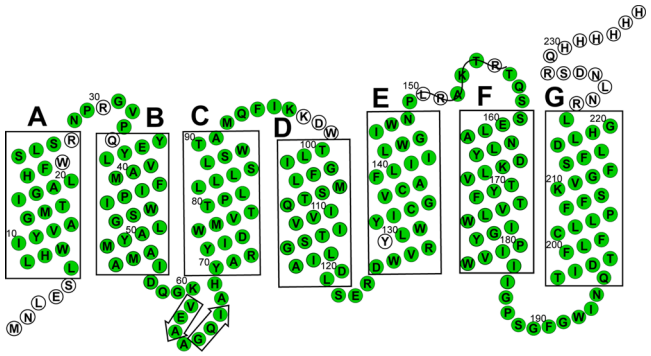

Figure 1. Amino acid sequence, secondary structure, and spectroscopic assignments of ASR. Transmembrane helices are represented by rectangles and designated by letters (A, B, etc.). Assigned residues are shown in green.[54] Cytoplasmic side is on top.

dipolar couplings D_{rigid} for N−H and C−H bonds were calculated using $^{15}N-^{1}H$ and $^{13}C-^{1}H$ bond lengths of 1.01 and 1.10 Å, respectively, as determined by neutron diffraction.[80]

Peak amplitudes extracted from ZF-TEDOR experiments as a function of dipolar evolution time were fit to the analytical expression described by Jaroniec, Griffin, and co-workers[62] and summarized in the Supporting Information. Simulations were performed on an $^{15}N_2-^{13}C$ three-spin system, which included coupling to a distant ^{15}N (e.g., $^{13}C_{\alpha}[i]$ coupled to the nitrogen $^{15}N[i+1]$ of the next residue at a distance of 2.41 Å or $^{13}C'[i]$ coupled to $^{15}N[i]$ at 2.45 Å). The effects of finite length 180° ^{15}N pulses were accounted for by using a theoretical scaling factor of 0.974 for the dipolar interactions, calculated according to the rotor period and the pulse length.[81] Fit parameters were overall amplitude, relaxation time, and the one-bond $^{15}N-^{13}C$ dipolar coupling. The rigid limit dipolar coupling constants were calculated using the standard one-bond lengths of 1.46 and 1.33 Å for N−C_{α} and N−C′ bonds, respectively.[79]

For the analysis of relaxation rates in the rotating frame ($R_{1\rho}$) 2D NCA spectra were processed in NMRPipe with Gaussian window functions using two different parameter sets to increase the number of resolved residues. First, 40 Hz line broadening and 80 Hz line sharpening in the direct dimension and 40 Hz line broadening and 90 Hz line sharpening in the indirect dimension were used to increase resolution of overlapped regions. In the second type of processing, 40 Hz line broadening and 70 Hz line sharpening in both the direct and indirect dimensions were used to improve the signal-to-noise ratios of isolated peaks. $R_{1\rho}$ trajectories were fit to single exponentials.

Error Analysis. Statistical analysis of random errors was performed using in-house Monte Carlo simulations implemented using the C programing language. Briefly, for each of the data sets, the best fit to the experimental data was first determined using the corresponding theoretical model. Random noise was simulated according to a Gaussian distribution with a standard deviation equal to that of the root-mean-square (rms) of spectral noise. Simulated noise was added to the best-fit points, and the resulting set was refit. This procedure was repeated 5000 times, and the resulting distributions of fit parameters were used to estimate random errors.

Systematic errors originating from pulse imperfections and RF inhomogeneity were estimated using simulations implemented in Spinevolution.[82] In TMREV experiments, it was found that a ^{1}H RF power level error of 5%, resulting from RF inhomogeneity or calibration uncertainty, would result in a 3% error in the observed order parameter. In ZF-TEDOR experiments, an ^{15}N RF power level error of 5% would only result in a 0.6% error in the observed order parameter. In general, systematic errors were much smaller than the random errors.

RESULTS

Probing Dipolar Order Parameters. The 3D CONCA experiment provides nearly complete resolution of the

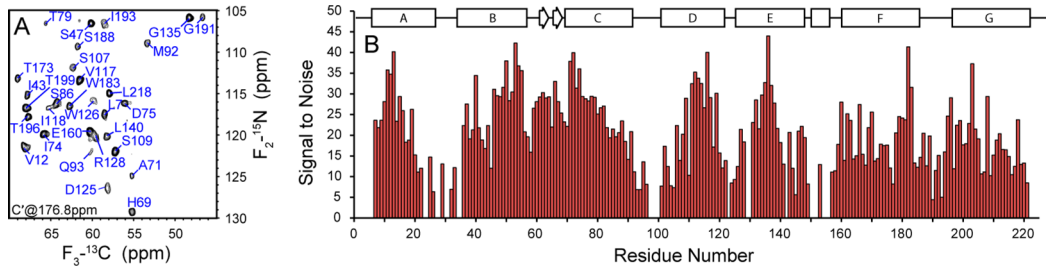

Figure 2. Three-dimensional CONCA spectroscopy. (A) Representative F_2−F_3 (NCA) 2D plane of a 3D CONCA experiment. Cross-peaks are labeled according to the $^{15}N/^{13}C_\alpha$ assignments. (B) Signal-to-noise ratios of individual cross-peaks detected in a 3D CONCA experiment conducted on UCN ASR are plotted as a function of residue number. The spectrum was recorded at a proton frequency of 800 MHz as described previously.[48] The secondary structure of lipid-reconstituted ASR is shown on top.[7]

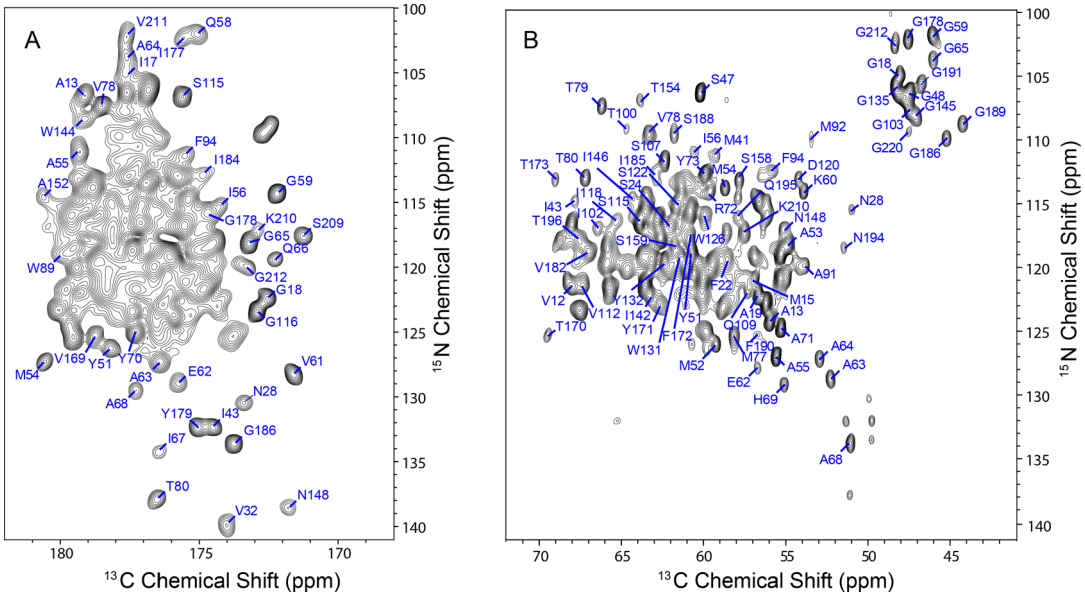

Figure 3. Representative two-dimensional spectra of ASR collected at 600 MHz. (A) Two-dimensional NCO spectrum acquired on 1,3-ASR using the pulse sequence shown in Figure S2 with a ZF-TEDOR mixing time of 1.33 ms (16 rotor cycles). The first contour is cut at 10 × σ, with each additional level multiplied by 1.2. Spectra for each TEDOR mixing point were collected with 64 scans and a recycle delay of 2.0 s, resulting in a total experimental time of 7.7 h for each two-dimensional spectrum. (B) Two-dimensional NCA spectrum acquired on 2-ASR with cross-polarization used for $^{15}N/^{13}C$ mixing. This spectrum was collected using the pulse sequence shown in Figure S1B, without TMREV mixing. Spectra for each TMREV mixing point were collected with 40 scans and a recycle delay of 2.9 s, resulting in a total experimental time of 7.3 h for each two-dimensional spectrum. Blue labels represent cross-peak assignments for all resolved residues (BMRB entry 18595).

backbone sites $^{13}C'$, ^{15}N, and $^{13}C_\alpha$ (Figure 2A) and allows site-specific investigation of the polarization transfer efficiencies as a preliminary indicator of the local protein mobility. The sequential plot of cross-peak intensities in Figure 2B shows that on average the transmembrane regions appear to be more rigid, while signal attenuation in the solvent-exposed flanks of helices and in the loops on the cytoplasmic side (loops A−B, C−D, E−F) indicates their possible increased mobility. In contrast, the extracellular side is more rigid. Specifically, we do not observe significant attenuation of relative cross-peak intensities in a short but well-defined β-hairpin in the B−C loop.[7] While the D−E and F−G loops have lower signal intensities, the signals from these loops are overall stronger than from those on the cytoplasmic side and in the case of the F−G loop are comparable with intensities observed in helices F and G.

Interestingly, there is a notable intensity variation even for residues within the same TM helix, indicating that motional averaging of the dipolar interactions is not the only factor responsible for the polarization transfer efficiency. Some contributing factors may be related to the variation in local proton density and decoupling performance, as well as possible proton $T_{1\rho}$ dispersion. To obtain a more detailed, site-specific view of the backbone order in ASR, we used 3D DIPSHIFT correlation spectroscopy to measure residue-specific dipolar order parameters. Four dipolar couplings per residue were measured to characterize the backbone flexibility: ^{15}N−^1H_N, $^{13}C_\alpha$−$^1H_\alpha$, $^{13}C'$−^{15}N, and $^{13}C_\alpha$−^{15}N. Each coupling was determined in a separate 3D experiment consisting of a series of 2D backbone chemical shift correlation experiments, NCA or NCO, recorded as a function of the dipolar evolution time. The dipolar interactions were recoupled using the TMREV sequence to probe ^{15}N−^1H and $^{13}C_\alpha$−^1H interactions and ZF-TEDOR to measure ^{15}N−$^{13}C_\alpha$ and ^{15}N−$^{13}C'$ dipolar interactions.

The resulting dipolar trajectories (i.e., the dependence of cross-peak intensities on the dipolar evolution time) are largely dependent on the strongest one-bond dipolar coupling of interest, which can be reduced by local motions, occurring on a time scale on the order or faster than the reciprocal of the

dx.doi.org/10.1021/ja411633w | J. Am. Chem. Soc. 2014, 136, 2833−2842

probed interaction. The dipolar order parameters, defined as ratios between the experimental dipolar couplings and the rigid limit, $\langle S \rangle = D_{expt}/D_{rigid}$, are sensitive measures of the amplitudes of motions (but insensitive to the time scale, as long as it is faster than the inverse of the measured interaction). These motions are often visualized as a diffusion cone defined by the semiangle θ related to the order parameter as $\langle S \rangle = 1/2 \cos\theta(1 + \cos\theta)$.

As the spectral resolution of 2D NCA and NCO spectra is not sufficiently high in uniformly ^{13}C,^{15}N-labeled ASR, we recorded our data on alternately labeled samples, 1,3-ASR and 2-ASR. In Figure 3, we show representative 2D NCO and NCA spectra demonstrating the resolution and sensitivity of these experiments. Cumulatively, a total of 92 $^{15}N-^{1}H$ and 68 $^{13}C_\alpha-^{1}H_\alpha$ dipolar couplings corresponding to cross-peaks with signal-to-noise ratios (SNR) of at least 15 could be measured in these samples. Additionally, a total of 75 $^{15}N-^{13}C_\alpha$ and 50 $^{15}N-^{13}C'$ couplings could be resolved in ZF-TEDOR-based correlation spectra. These couplings are evenly distributed along the protein sequence and can be used for characterization of the dipolar order parameters in ASR.

Figure 4A shows representative $^{15}N-^{13}C_\alpha$ ZF-TEDOR dipolar buildup curves for S47, located in the transmembrane

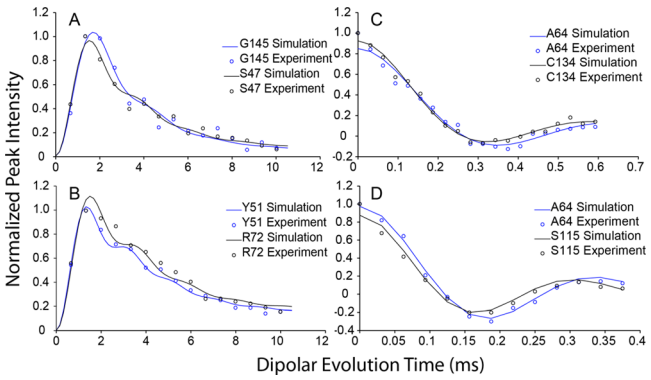

Figure 4. Representative dipolar trajectories measured in 3D DIPSHIFT experiments. All data were recorded at 600 MHz, using 12 kHz magic angle spinning in TEDOR experiments and 8 kHz in TMREV experiments. (A,B) Experimental 3D TEDOR buildup curves (open circles) and best-fit simulations (solid lines) for (A) $^{15}N-^{13}C_\alpha$ and (B) $^{15}N-^{13}C'$ couplings. (C,D) Experimental 3D TMREV dephasing curves (open circles) and best fits (solid lines) for (C) $^{1}H-^{15}N$ and (D) $^{1}H-^{13}C$ couplings. TMREV was implemented with 4 MREV elements per rotor cycle. Additional details of simulations and best fits can be found in the Experimental Section.

portion of helix B, and G145, found approximately one turn below the cytoplasmic end of helix E. Similar to most other residues, the $N-C_\alpha$ bond in S47 is rigid with the corresponding order parameter $\langle S \rangle$ being close to unity. G145 shows a slightly slower buildup but overall is quite rigid, as well, with a best-fit order parameter $\langle S \rangle = 0.87$. Likewise, the trajectories for the $^{15}N-^{13}C'$ peptide bond dipolar couplings for TM residue Y51, found in helix B, and R72, located on the extracellular side of helix C, exhibit similar time scales of the TEDOR buildup (Figure 4B).

Representative TMREV dephasing curves are shown in Figure 4C,D for residues S115 and C134, located in helices D and E, and for A64, located in the B−C loop. Both S115 and C134 residues exhibit fairly restricted motions on the submicrosecond time scale with average order parameters of 0.97. On the other hand, the N−H and $C_\alpha-H_\alpha$ bonds of A64, which are located in the region connecting the two short β-strands, V61−A63 and Q66−A68,[7] undergo motions of larger amplitudes, with average order parameters for both $^{15}N-^{1}H$ and $^{13}C_\alpha-^{13}H_\alpha$ of 0.89.

Detailed residue-specific analysis of the 3D TMREV and ZF-TEDOR DIPSHIFT experiments is shown in Figure 5. The $\langle S \rangle$ values show quite featureless profile for both $C_\alpha-H_\alpha$ and N−H bonds (Figure 5A,B), with the majority of residues exhibiting dipolar order parameters in the range between 0.9 and 1.0 for both types of couplings. While some loop regions (e.g., B−C and F−G loops) have lower order parameters and appear to experience less restricted motions on the submicrosecond time scale, the protein backbone appears to be quite rigid overall.

A similar pattern is observed for the $^{13}C_\alpha-^{15}N$ effective coupling strengths, which are sensitive to submillisecond motions of the backbone. The majority of $C_\alpha-N$ order parameters fall in the range between 0.90 and 1.05. Lower $\langle S \rangle$ values are observed in the cytoplasmic A−B loop for P29 ($\langle S \rangle = 0.88$) and in the E−F loop for G145 ($\langle S \rangle = 0.87$). The C′−N peptide bond order parameters are, on average, narrowly clustered in the range from 0.8 to 0.9, indicating little variation in the peptide bond geometry across the protein, while the overall reduction is likely related to a systematic error in the peptide bond length used for the calculation of the rigid limit.

Probing Slow Dynamics by ^{15}N $R_{1\rho}$ Measurements. To ascertain the extent of motions, we performed ^{15}N transverse relaxation rate measurements. The NMR spin−lattice relaxation, R_2, or the spin−lattice relaxation in the rotating frame, $R_{1\rho}$, are sensitive reporters on motions occurring on an intermediate, nanosecond−microsecond time scale. Although in the solid-state these relaxation rates are typically dominated by the coherent contributions, it was recently demonstrated that these contributions to $R_{1\rho}$ relaxation rates are effectively suppressed under fast MAS (spinning frequencies greater than 45 kHz) and with the ^{15}N spinlock RF strength greater than 10 kHz (and away from rotary recoupling conditions[73,74]). Under these conditions, $R_{1\rho}$ rates are dominated by stochastic contributions.[34]

Spin−lattice ^{15}N $R_{1\rho}$ rotating frame relaxation rate measurements were conducted at a spinning frequency of 50 kHz using a 1.3 mm MAS probe. To confirm that fast MAS suppresses coherent contributions and results in significantly smaller relaxation rates in membrane proteins reconstituted in a lipid environment, we initially estimated bulk $R_{1\rho}$ as a function of the lock field, as shown in Figure 6. In qualitative agreement with the results obtained on GB1,[34] we observed a significant decrease in relaxation rates with increasing spinlock field, with $R_{1\rho}$ reaching a plateau at ~2.8 s^{-1} ($T_{1\rho} \sim 360$ ms) at spinlock fields higher than ~10 kHz.

Site-specific $R_{1\rho}$ measurements were performed at four spinlock power levels (10, 12, 14, 16 kHz), and all measurements gave similar results within confidence intervals. In Figure 7, we show a representative NCA correlation spectrum of UCN ASR.

Because of the reduced amount of sample in a 1.3 mm rotor, the large molecular weight of the protein, and the presence of lipids, site-specific relaxation measurements are impeded by low sensitivity, allowing us to reliably extract intensities and estimate relaxation rates for a total of 53 residues. Representative $R_{1\rho}$ decay curves for transmembrane residues (T170, Y171) and for those found at the exposed flanks of helices (A71) and in the loops (K60 and Q66 in the B−C loop,

dx.doi.org/10.1021/ja411633w | J. Am. Chem. Soc. 2014, 136, 2833−2842

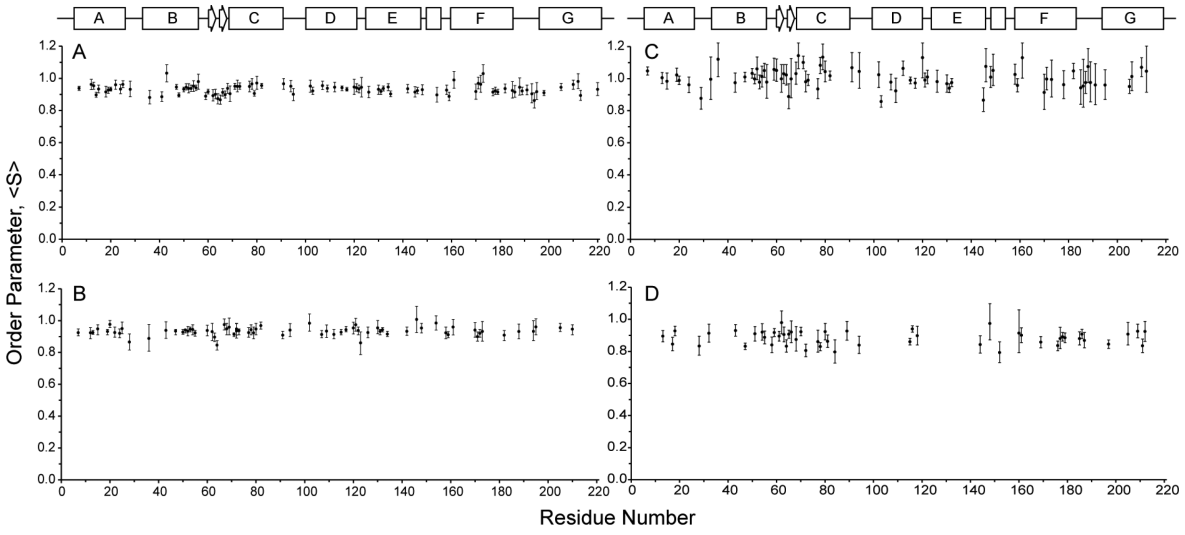

Figure 5. One-bond order parameters for $^{1}H-^{15}N$ (A), $^{1}H_{\alpha}-^{13}C_{\alpha}$ (B), $^{15}N-^{13}C_{\alpha}$ (C), and $^{15}N-^{13}C'$ (D) couplings as functions of residue number. Residue number for the peptide bond order parameters in (D) is defined according to the carbonyl. For each of the measured couplings, the dipolar order parameters were defined as ratios $\langle S\rangle = D_{expt}/D_{rigid}$, where D_{expt} are experimentally determined dipolar couplings, and D_{rigid} represents the rigid limit calculated using bond lengths of 1.01 Å for N–H, 1.10 Å[80] for $C_{\alpha}-H_{\alpha}$, 1.46 Å for $N-C_{\alpha}$, and 1.33 Å for $N-C'$.[79]

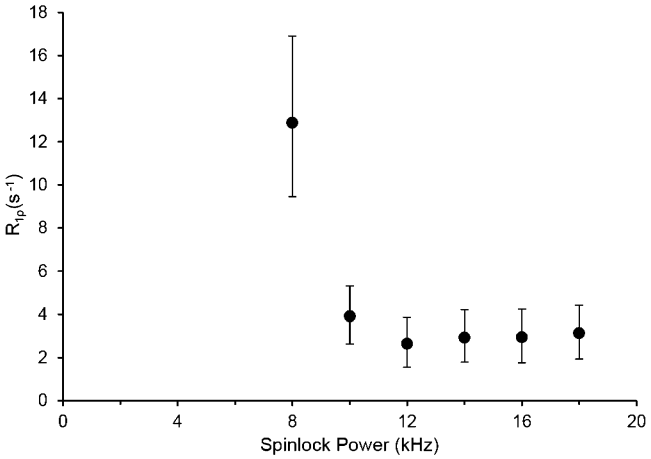

Figure 6. Bulk amide ^{15}N $R_{1\rho}$ as a function of the spinlock field strength. Data were recorded at 800 MHz and at a spinning frequency of 50 kHz. The data are in qualitative agreement with Lewandowski et al.[34]

and Q195 in the F–G loop) are shown in Figure 7B,C. Vastly different relaxation rates extracted from these curves, varying by almost an order of magnitude, underscore the widely different dynamic regimes for different parts of the protein.

In Figure 8A, we show the ^{15}N $R_{1\rho}$ relaxation rates plotted as a function of residue number. While the detected $R_{1\rho}$ rates for the transmembrane regions are in the range of a few inverse seconds, much higher values were measured for some of the loops, as well as for a few isolated residues at the ends of α-helices. Remarkably, we observe significantly elevated relaxation rates for residues in the B–C loop (residues G59-K60, E62-Q66, A68-H69, Figure 8A), as well as for I185, S188, and G189 in the extracellular F–G loop, indicating an additional slow motional regime which dominates the stochastic fluctuations responsible for the transverse relaxation processes. Faster relaxation rates are also detected for E36 ($R_{1\rho}$ = 10.5 s^{-1}) and N148 ($R_{1\rho}$ = 9.5 s^{-1}), which are located in the cytoplasmic flanks of helices B and E, respectively, indicating that the A–B and E–F loops may be subjected to slower motions, as well.

To gain insight into the time scale of motions dominating the relaxation pathways in ASR, we used the theoretical model developed by Kurbanov et al.[83] This model provides estimates for $R_{1\rho}$ relaxation rates for a spin I (^{15}N) subjected to chemical shift anisotropy and coupled through space to another spin S (^{1}H) in the presence of MAS:

$$R_{1\rho} = \frac{1}{2}R_1^{CSA} + \frac{1}{2}R_1^{IS} + R_{1\Delta}^{CSA} + R_{1\Delta}^{IS} \quad (1)$$

where R_1^{CSA} and R_1^{IS} are the longitudinal relaxation rates resulting from the anisotropic chemical shift and dipolar coupling, and $R_{1\Delta}^{CSA}$ and $R_{1\Delta}^{IS}$ are the additional dependence on the transverse relaxation rate. Approximating the CSA tensor as axially symmetric, these contributions can be written as follows (full expressions for the general case can be found in ref 83):

$$R_1^{CSA} = \frac{3}{4}(\delta\omega_I)^2 J(\omega_I) \quad (2)$$

$$R_1^{IS} = (b_{IS}/2)^2 (J(\omega_I - \omega_S) + 3J(\omega_I) + 6J(\omega_I + \omega_S)) \quad (3)$$

$$R_{1\Delta}^{CSA} = \frac{1}{6}(\delta\omega_I)^2 \left\{ \frac{1}{2}J(\omega_I - 2\omega_R) + J(\omega_I - \omega_R) + J(\omega_I + \omega_R) + \frac{1}{2}J(\omega_I + 2\omega_R) \right\} \quad (4)$$

$$R_{1\Delta}^{IS} = \frac{1}{6}(b_{IS}/2)^2 \left\{ 3J(\omega_S) + \frac{1}{3}J(\omega_I - 2\omega_R) + \frac{2}{3}J(\omega_I - \omega_R) + \frac{2}{3}J(\omega_I + \omega_R) + \frac{1}{3}J(\omega_I + 2\omega_R) \right\} \quad (5)$$

Here, ω_1 is the spinlock field strength expressed in rad/s (we neglect small off-resonance effects), $\omega_R/2\pi$ is the spinning frequency, and ω_S and ω_I are the Larmor frequencies of the two nuclei, ^{1}H and ^{15}N; b_{IS} is the strength of the dipolar coupling, and δ is the chemical shift anisotropy, for which we used a value

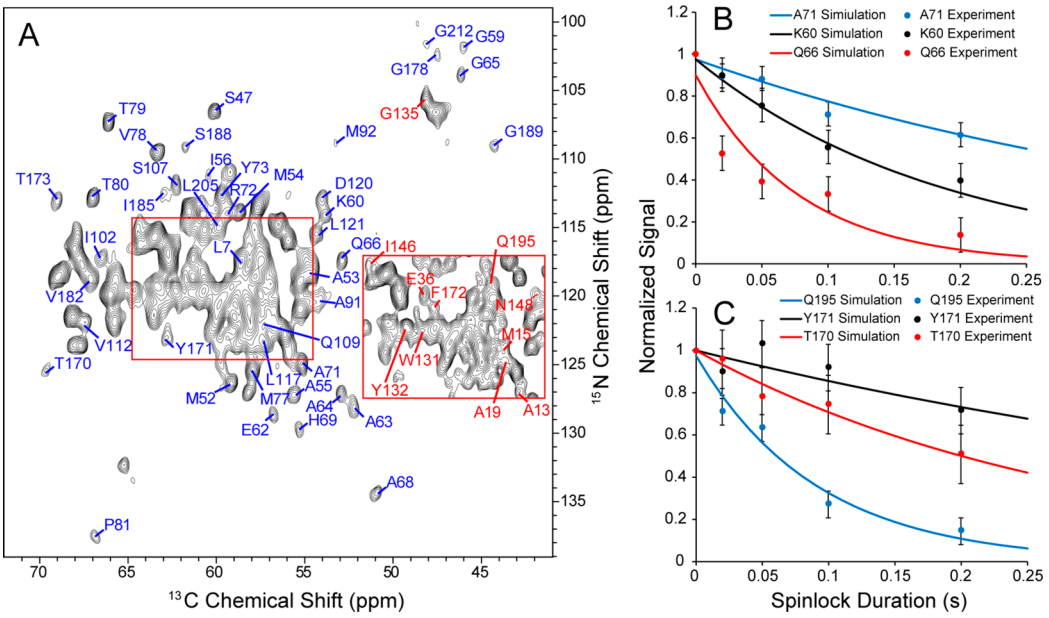

Figure 7. (A) Representative 2D NCA correlation spectrum of UCN ASR collected at 800 MHz and at a spinning frequency of 50 kHz. Acquisition length in the indirect ^{15}N dimension was 11.6 ms, and the total experimental time for a single 2D spectrum was 11−13 h. Spectra were processed in two ways. A Lorentzian-to-Gaussian window function with line narrowing of 80 Hz and line broadening of 40 Hz in the direct dimension and with 90 Hz line narrowing and 40 Hz of line broadening in the indirect dimension was used to increase resolution of overlapped cross-peaks (shown as an inset). A Lorentzian-to-Gaussian window function with line narrowing of 70 Hz and line broadening of 40 Hz in both the direct and indirect dimension was used to increase the signal-to-noise of isolated peaks. Red labels indicate resonances that could be resolved with the first type of processing. (B) Representative $R_{1\rho}$ trajectories and best fits for A71, located on the extracellular side of helix C ($R_{1\rho}$ = 2.3 s^{-1}), K60, located in the unstructured part of the B−C loop ($R_{1\rho}$ = 5.3 s^{-1}), and Q66, found at the end of the second β-strand within the B−C loop ($R_{1\rho}$ = 13.0 s^{-1}). (C) Representative $R_{1\rho}$ trajectories and best fits for T170 ($R_{1\rho}$ = 3.5 s^{-1}) and Y171 ($R_{1\rho}$ = 2.4 s^{-1}) located on the extracellular side of helix F and Q195 ($R_{1\rho}$ = 11.0 s^{-1}) located on the extracellular side of helix G.

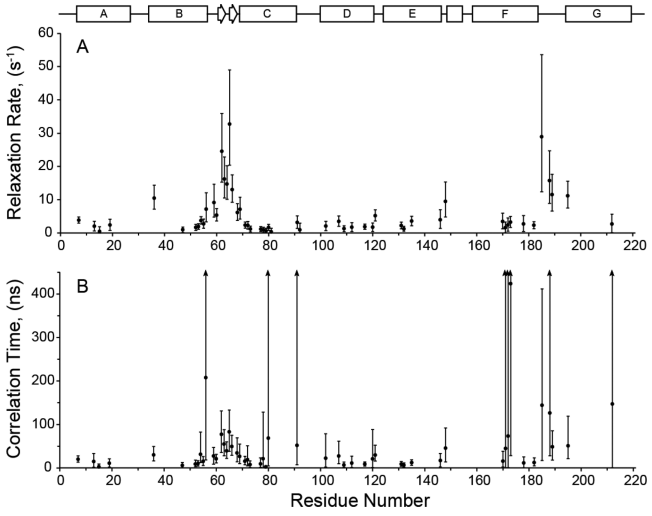

Figure 8. (A) Site-specific $R_{1\rho}$ relaxation rate constants determined at 12 kHz spinlock power, and (B) motional correlation times estimated using single exponential autocorrelation function approximation as discussed in the text. Error bars define a 95% confidence level interval. Arrows indicate cases where only the lower bound on the correlation time could be extracted.

of 97.7 ppm in our calculations.[84] Variation in ^{15}N chemical shift anisotropy reported earlier[85] was found to result in a small variation in the correlation time, well within the confidence intervals. $J(\omega)$ is the spectral density function, which is directly related to motional parameters such as the correlation time τ_c, and the order parameter S describing the amplitude of motion:

$$J(\omega) = \frac{2}{5}(1 - S^2)\frac{\tau_c}{1 + \omega^2\tau_c^2} \quad (6)$$

ASR likely undergoes conformational fluctuations and motions in a wide range of time scales, ranging from fast picosecond time scale local motions to much slower collective motions. The model employed here assumes a single exponential component in the autocorrelation function and can only be used to estimate the dominant contributions. In particular, we neglect the fast picosecond motions, which have almost negligible effect on $R_{1\rho}$ but may contribute significantly to averaging of dipolar couplings.[29,30,86] Moreover, the employed model neglects possible anisotropy of motions (discussed in the following). Thus, the extracted correlation times should be considered as estimates only. Figure 8B shows correlation times obtained using eqs 1−6. We observe motions within helices on the order of low tens of nanoseconds, whereas the B−C and F−G loops undergo almost an order of magntitude slower motions, on the tens to hundreds of nanosecond time scale.

The occurrence of the slow motions in the B−C and F−G loops offers an explanation to the observed dispersion of relaxation rates and also provides an additional insight into the dynamics of rhodopsins. The β-hairpin in the B−C loop is a conserved structural motif among many microbial rhodopsins,[87,88] suggesting that it may play similar roles in many members of the family. Among homologous proteins of 7TM architecture, bacteriorhodopsin (BR) is best characterized, both functionally, structurally, and dynamically. In BR, conformations of the B−C and F−G loops are related to the structure of the retinal binding pocket, affect proton translocation,[89] and

dx.doi.org/10.1021/ja411633w | J. Am. Chem. Soc. 2014, 136, 2833−2842

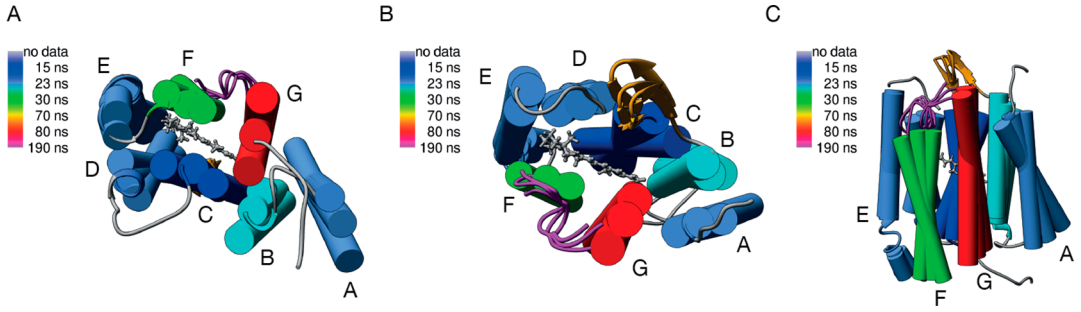

Figure 9. Time scales, amplitudes, and directions of motions obtained from fitting $R_{1\rho}$, S^2_{NH}, and $S^2_{C\alpha H\alpha}$ to anisotropic collective motions of secondary structure elements of ASR, (A) viewed from the cytoplasmic side, (B) viewed from the extracellular side, and (C) side view. The effective time scale is indicated with color. The amplitudes and directions of motions are indicated with conformations corresponding to rotation extremes from the average position. Pivot points for the rotations are arbitrary. Helices are rendered as pipes. Motional parameters are shown for a single monomer only.

play a role in the final folding step and formation of the Schiff base between the retinal and Lys216.[90] Neutralization of the negative charge of the Schiff base counterion by low pH or by mutation results in disordering of the B−C loop as does the removal of the retinal, pointing at the coupling of this loop to the chromophore.[16,91−93] Previous solid-state NMR measurements on bacteriorhodopsin indicated large amplitude motions in the B−C loop,[94] while EPR data suggested a time scale of ∼200 ns,[95] which is in a qualitative agreement with the time scale estimated in ASR.

While the ordered structure of the B−C loop appears to be preserved at least in some of the photointermediate states of BR,[96] the overall collective mobility of this loop may be required for adaptation to the structural changes occurring in the retinal pocket during the photocycle. This is likely even more important for ASR, where conformational changes characterizing the ASRT-bound and unbound states are expected to be larger. Similarly, the flexible F−G loop in ASR may serve as a hinge point for the movement of helix G proposed by us earlier,[57] and as was shown for some BR photointermediates.[97,98]

Overall slow times scales of motions estimated for helices (∼tens of nanoseconds in many cases) and especially fo the B−C and F−G loops suggest the possibility of collective, possibly anisotropic, motions in the protein, which could under favorable conditions dominate the relaxation pathways.[41,99,100] Indeed, transmembrane helices of ASR are stabilized by intrahelical hydrogen bonds and structurally well-defined. The B−C loop consists of two well-defined antiparallel β-strands according to the chemical shift index analysis,[48] as well as structural measurements.[7] CSI analysis and the hydrogen−deuterium exchange pattern for the F−G loop[7] suggest the possibility of defined structural elements in this loop, as well. In order to investigate whether the measured data could be explained by collective motions, we considered a simple model where the overall motions of secondary structure elements are approximated as rigid body motions with a single time scale and three amplitudes parametrized as Gaussian fluctuations against three orthogonal axes. The expressions for relaxation rates, which are used in this model, are identical to the ones presented in eqs 1−6, with the exception of the order parameter S^2, which is replaced by a 3D Gaussian axial fluctuation (3D GAF) order parameter[101] for the bond vectors expressed in a common reference frame for the overall motion (for details, see Supporting Information).

In the implementation of fitting procedures, helices and the B−C and F−G loops were considered independently. For each secondary structure element, the spherical coordinates for C_α−H_α and N−H bond vectors were expressed in a molecular frame, and all of the available $R_{1\rho}$, S^2_{NH}, and $S^2_{C\alpha H\alpha}$ were fitted simultaneously to a model with six fit parameters. Four of them, the time scale τ, and three amplitudes, σ_α, σ_β, σ_γ, directly describe collective motions. The additional two parameters, $\delta\theta$ and $\delta\phi$, describe transformation between the molecular and 3D GAF frame, which is not known a priori. $S^2_{NC\alpha}$ and S^2_{NCO} were not considered in the fitting procedure because some of the N−C_α order parameters obtained from ZF-TEDOR measurements are larger than 1, which may indicate a presence of an unaccounted for systematic offset. Such an offset does not affect the validity of qualitative comparisons of amplitudes of motions for different residues but may lead to a significant bias in quantitative analysis. Once again, we explicitly neglected local picosecond motions, which contribute to the measured dipolar order parameters. Thus, the correlation times obtained with such fitting should be treated as effective time scales (most likely faster than the time scale of the actual fluctuations), and the amplitudes for the overall slow motions are likely overestimated.

The time scales, amplitudes, and directions of motions obtained using the above-described model are depicted in Figure 9 and detailed in Table S4. The anisotropic collective motions account well for the measured relaxation rates and dipolar order parameters (reduced χ^2 of the fits are often close to 1), suggesting that the collective motion of molecular fragments is a good model for explaining most of our data. The fits are better for helices, which are well structured and more likely to be better approximated by rigid body motions than loops. As the amplitudes obtained using the 3D GAF approach are constrained primarily by the dipolar order parameters, and the estimation of time scales relies heavily on $R_{1\rho}$ measurements, the time scale for the motion of helix G is likely to be the least reliable, as only two $R_{1\rho}$ values are available for the entire fragment.

Overall, the time scales of collective motions determined using the 3D GAF model correlate with the time scales determined from the site-specific analysis. Six helices (A−F) are characterized by similar effective time scales on the order of ∼20−30 ns. The motion of the seventh helix G is the slowest (effective time scale on the order of 90 ns), which may be due to the additional steric constraints resulting from interactions between a retinal cofactor attached to helix G and other helices.

dx.doi.org/10.1021/ja411633w | J. Am. Chem. Soc. 2014, 136, 2833−2842

The B−C and F−G loops undergo slower motions on the time scale of 70 and 190 ns, respectively, in agreement with the site-specific analysis.

CONCLUSIONS

In summary, we have studied the conformational dynamics of the 7TM photoreceptor *Anabaena* Sensory Rhodopsin. We used three-dimensional dipolar chemical shift correlation spectroscopy to determine the effective one-bond dipolar order parameters and characterized the amplitudes of sub-microsecond time scale motions in the protein. We have found that, for the detected residues, the $^{15}N-^{1}H_N$ and $^{13}C_\alpha-^{1}H_\alpha$ dipolar order parameters are close to unity, indicating that both the TM and exposed regions of the protein undergo restricted motions on the submicrosecond time scale. Although more variation is detected in the $^{13}C_\alpha-^{15}N$ and $^{13}C'-^{15}N$ effective dipolar couplings, which characterize the amplitudes of molecular fluctuations of the ϕ and ω torsion angles, these motions appear to be quite restricted for the majority of residues, as well.

Dipolar order parameters do not directly report on the time scale of motions, and we employed ^{15}N spin−lattice rotating frame relaxation measurements under fast MAS to probe intermediate molecular motions in ASR. Relaxation rates found for the B−C and F−G loops on the extracellular side are almost an order of magnitude greater than the values detected for the transmembrane regions, indicating the increased contribution of slower motions to the relaxation rates. Using the 3D GAF approach, the relaxation rates and order parameters could be explained by a model assuming collective motions of molecular fragments (e.g., entire helices or loops). Remarkably, our data suggest that both the transmembrane regions traditionally considered as rigid and more flexible solvent-exposed domains may undergo rigid body motions on a time scale of tens to hundreds of nanoseconds. ASR is unique among microbial rhodopsins in that it is the only one known so far to interact with a soluble transducer, which bears some similarity to the initial step in the signal transduction cascade employed by G-protein-coupled receptors (GPCRs). Interestingly, recently published normal mode analyses of the agonist-bound β2-adrenergic receptor suggested that the receptor could experience a large number of motions in the absence of transducer. In contrast, the GPCR bound to G-protein was found to be much more motionally restricted.[102] SSNMR measurements extended to the ASR:ASRT complex would help identify if binding the transducer will have similar restrictive effect on the collective motions in ASR.

ASSOCIATED CONTENT

Supporting Information

Experimental pulse sequences, data analysis procedures, tables of experimentally determined order parameters, $R_{1\rho}$ relaxation rates, and extracted motional amplitudes and correlation times. This material is available free of charge via the Internet at http://pubs.acs.org.

AUTHOR INFORMATION

Corresponding Author

vladizha@uoguelph.ca

Present Address

[‖]Beijing NMR Center, Peking University, Beijing, China.

Notes

The authors declare no competing financial interest.

ACKNOWLEDGMENTS

This research was supported by the Natural Sciences and Engineering Research Council of Canada (Discovery Grants to V.L. and L.S.B.), the Canada Foundation for Innovation, and the Ontario Ministry of Economic Development and Innovation. V.L. holds a Canada Research Chair in Biophysics. D.G. is a recipient of an Ontario Graduate Scholarship. J.R.L. is supported by startup funds from the University of Warwick.

REFERENCES

(1) Tate, C. G.; Schertler, G. F. *Curr. Opin. Struct. Biol.* **2009**, *19*, 386.
(2) Hu, F.; Luo, W.; Hong, M. *Science* **2010**, *330*, 505.
(3) Sharma, M.; Yi, M.; Dong, H.; Qin, H.; Peterson, E.; Busath, D. D.; Zhou, H. X.; Cross, T. A. *Science* **2010**, *330*, 509.
(4) Lange, A.; Giller, K.; Hornig, S.; Martin-Eauclaire, M. F.; Pongs, O.; Becker, S.; Baldus, M. *Nature* **2006**, *440*, 959.
(5) Cady, S. D.; Schmidt-Rohr, K.; Wang, J.; Soto, C. S.; Degrado, W. F.; Hong, M. *Nature* **2010**, *463*, 689.
(6) Park, S. H.; Das, B. B.; Casagrande, F.; Tian, Y.; Nothnagel, H. J.; Chu, M.; Kiefer, H.; Maier, K.; De Angelis, A. A.; Marassi, F. M.; Opella, S. J. *Nature* **2012**, *491*, 779.
(7) Wang, S.; Munro, R. A.; Shi, L.; Kawamura, I.; Okitsu, T.; Wada, A.; Kim, S. Y.; Jung, K. H.; Brown, L. S.; Ladizhansky, V. *Nat. Methods* **2013**, *10*, 1007.
(8) Franks, W. T.; Zhou, D. H.; Wylie, B. J.; Money, B. G.; Graesser, D. T.; Frericks, H. L.; Sahota, G.; Rienstra, C. M. *J. Am. Chem. Soc.* **2005**, *127*, 12291.
(9) Etzkorn, M.; Martell, S.; Andronesi, O. C.; Seidel, K.; Engelhard, M.; Baldus, M. *Angew. Chem., Int. Ed.* **2007**, *46*, 459.
(10) Shi, L.; Lake, E. M.; Ahmed, M. A.; Brown, L. S.; Ladizhansky, V. *Biochim. Biophys. Acta* **2009**, *1788*, 2563.
(11) Helmus, J. J.; Surewicz, K.; Nadaud, P. S.; Surewicz, W. K.; Jaroniec, C. P. *Proc. Natl. Acad. Sci. U.S.A.* **2008**, *105*, 6284.
(12) Yang, J.; Aslimovska, L.; Glaubitz, C. *J. Am. Chem. Soc.* **2011**, *133*, 4874.
(13) Higman, V. A.; Varga, K.; Aslimovska, L.; Judge, P. J.; Sperling, L. J.; Rienstra, C. M.; Watts, A. *Angew. Chem., Int. Ed.* **2011**, *50*, 8432.
(14) Yang, J.; Tasayco, M. L.; Polenova, T. *J. Am. Chem. Soc.* **2009**, *131*, 13690.
(15) Lorieau, J. L.; McDermott, A. E. *J. Am. Chem. Soc.* **2006**, *128*, 11505.
(16) Lorieau, J. L.; Day, L. A.; McDermott, A. E. *Proc. Natl. Acad. Sci. U.S.A.* **2008**, *105*, 10366.
(17) Helmus, J. J.; Surewicz, K.; Surewicz, W. K.; Jaroniec, C. P. *J. Am. Chem. Soc.* **2010**, *132*, 2393.
(18) Vogel, A.; Katzka, C. P.; Waldmann, H.; Arnold, K.; Brown, M. F.; Huster, D. *J. Am. Chem. Soc.* **2005**, *127*, 12263.
(19) Palmer, A. G., III. *Chem. Rev.* **2004**, *104*, 3623.
(20) Jarymowycz, V. A.; Stone, M. J. *Chem. Rev.* **2006**, *106*, 1624.
(21) Palmer, A. G., III; Massi, F. *Chem. Rev.* **2006**, *106*, 1700.
(22) Torchia, D. A. *Annu. Rev. Biophys. Biol.* **1984**, *13*, 125.
(23) Ketchem, R. R.; Hu, W.; Tian, F.; Cross, T. A. *Structure* **1994**, *2*, 699.
(24) Watt, E. D.; Rienstra, C. M. *Anal. Chem.* **2014**, *86*, 58.
(25) McDermott, A. *Annu. Rev. Biophys.* **2009**, *38*, 385.
(26) Krushelnitsky, A.; Reichert, D.; Saalwachter, K. *Acc. Chem. Res.* **2013**, *46*, 2028.
(27) Krushelnitsky, A.; Zinkevich, T.; Reichert, D.; Chevelkov, V.; Reif, B. *J. Am. Chem. Soc.* **2010**, *132*, 11850.
(28) Zinkevich, T.; Chevelkov, V.; Reif, B.; Saalwachter, K.; Krushelnitsky, A. *J. Biomol. NMR* **2013**, *57*, 219.
(29) Schanda, P.; Meier, B. H.; Ernst, M. *J. Am. Chem. Soc.* **2010**, *132*, 15957.
(30) Chevelkov, V.; Fink, U.; Reif, B. *J. Biomol. NMR* **2009**, *45*, 197.

(31) Krushelnitsky, A.; Brauniger, T.; Reichert, D. *J. Magn. Reson.* **2006**, *182*, 339.
(32) Giraud, N.; Blackledge, M.; Bockmann, A.; Emsley, L. *J. Magn. Reson.* **2007**, *184*, 51.
(33) Lewandowski, J. R.; Sein, J.; Sass, H. J.; Grzesiek, S.; Blackledge, M.; Emsley, L. *J. Am. Chem. Soc.* **2010**, *132*, 8252.
(34) Lewandowski, J. R.; Sass, H. J.; Grzesiek, S.; Blackledge, M.; Emsley, L. *J. Am. Chem. Soc.* **2011**, *133*, 16762.
(35) Cady, S. D.; Goodman, C.; Tatko, C. D.; DeGrado, W. F.; Hong, M. *J. Am. Chem. Soc.* **2007**, *129*, 5719.
(36) Bhate, M. P.; Wylie, B. J.; Tian, L.; McDermott, A. E. *J. Mol. Biol.* **2010**, *401*, 155.
(37) Park, S. H.; Casagrande, F.; Das, B. B.; Albrecht, L.; Chu, M.; Opella, S. J. *Biochemistry* **2011**, *50*, 2371.
(38) Saito, H.; Naito, A. *Biochim. Biophys. Acta* **2007**, *1768*, 3145.
(39) Soong, R.; Smith, P. E.; Xu, J.; Yamamoto, K.; Im, S. C.; Waskell, L.; Ramamoorthy, A. *J. Am. Chem. Soc.* **2010**, *132*, 5779.
(40) Struts, A. V.; Salgado, G. F.; Brown, M. F. *Proc. Natl. Acad. Sci. U.S.A.* **2011**, *108*, 8263.
(41) Lewandowski, J. R. *Acc. Chem. Res.* **2013**, *46*, 2018.
(42) Haller, J. D.; Schanda, P. *J. Biomol. NMR* **2013**, *57*, 263.
(43) Reif, B. *J. Magn. Reson.* **2012**, *216*, 1.
(44) Giraud, N.; Blackledge, M.; Goldman, M.; Bockmann, A.; Lesage, A.; Penin, F.; Emsley, L. *J. Am. Chem. Soc.* **2005**, *127*, 18190.
(45) Knight, M. J.; Pell, A. J.; Bertini, I.; Felli, I. C.; Gonnelli, L.; Pierattelli, R.; Herrmann, T.; Emsley, L.; Pintacuda, G. *Proc. Natl. Acad. Sci. U.S.A.* **2012**, *109*, 11095.
(46) Jung, K. H.; Trivedi, V. D.; Spudich, J. L. *Mol. Microbiol.* **2003**, *47*, 1513.
(47) Vogeley, L.; Sineshchekov, O. A.; Trivedi, V. D.; Sasaki, J.; Spudich, J. L.; Luecke, H. *Science* **2004**, *306*, 1390.
(48) Shi, L.; Kawamura, I.; Jung, K. H.; Brown, L. S.; Ladizhansky, V. *Angew. Chem., Int. Ed.* **2011**, *50*, 1302.
(49) Jung, K. H. *Photochem. Photobiol.* **2007**, *83*, 63.
(50) Wang, S.; Kim, S. Y.; Jung, K. H.; Ladizhansky, V.; Brown, L. S. *J. Mol. Biol.* **2011**, *411*, 449.
(51) Furutani, Y.; Kawanabe, A.; Jung, K. H.; Kandori, H. *Biochemistry* **2005**, *44*, 12287.
(52) Sineshchekov, O. A.; Trivedi, V. D.; Sasaki, J.; Spudich, J. L. *J. Biol. Chem.* **2005**, *280*, 14663.
(53) Strambi, A.; Durbeej, B.; Ferre, N.; Olivucci, M. *Proc. Natl. Acad. Sci. U.S.A.* **2010**, *107*, 21322.
(54) Wang, S.; Shi, L.; Okitsu, T.; Wada, A.; Brown, L. S.; Ladizhansky, V. *Biomol. NMR Assignments* **2013**, *7*, 253.
(55) Wang, S.; Munro, R. A.; Kim, S. Y.; Jung, K. H.; Brown, L. S.; Ladizhansky, V. *J. Am. Chem. Soc.* **2012**, *134*, 16995.
(56) Vogeley, L.; Trivedi, V. D.; Sineshchekov, O. A.; Spudich, E. N.; Spudich, J. L.; Luecke, H. *J. Mol. Biol.* **2007**, *367*, 741.
(57) Wang, S.; Shi, L.; Kawamura, I.; Brown, L. S.; Ladizhansky, V. *Biophys. J.* **2011**, *101*, L23.
(58) Linser, R.; Dasari, M.; Hiller, M.; Higman, V.; Fink, U.; Lopez del Amo, J. M.; Markovic, S.; Handel, L.; Kessler, B.; Schmieder, P.; Oesterhelt, D.; Oschkinat, H.; Reif, B. *Angew. Chem., Int. Ed.* **2011**, *50*, 4508.
(59) Ward, M. E.; Shi, L.; Lake, E.; Krishnamurthy, S.; Hutchins, H.; Brown, L. S.; Ladizhansky, V. *J. Am. Chem. Soc.* **2011**, *133*, 17434.
(60) Zhou, D. H.; Nieuwkoop, A. J.; Berthold, D. A.; Comellas, G.; Sperling, L. J.; Tang, M.; Shah, G. J.; Brea, E. J.; Lemkau, L. R.; Rienstra, C. M. *J. Biomol. NMR* **2012**, *54*, 291.
(61) Hing, A. W.; Vega, S.; Schaefer, J. *J. Magn. Reson.* **1992**, *96*, 205.
(62) Jaroniec, C. P.; Filip, C.; Griffin, R. G. *J. Am. Chem. Soc.* **2002**, *124*, 10728.
(63) Hohwy, M.; Jaroniec, C. P.; Reif, B.; Rienstra, C. M.; Griffin, R. G. *J. Am. Chem. Soc.* **2000**, *122*, 3218.
(64) Banigan, J. R.; Traaseth, N. J. *J. Phys. Chem. B* **2012**, *116*, 7138.
(65) Fung, B. M.; Khitrin, A. K.; Ermolaev, K. *J. Magn. Reson.* **2000**, *142*, 97.
(66) Ammann, C.; Meier, P.; Merbach, A. E. *J. Magn. Reson.* **1982**, *46*, 319.
(67) Thurber, K. R.; Tycko, R. *J. Magn. Reson.* **2009**, *196*, 84.
(68) Pines, A.; Gibby, M. G.; Waugh, J. S. *J. Chem. Phys.* **1973**, *59*, 569.
(69) Hartmann, S. R.; Hahn, E. L. *Phys. Rev.* **1962**, *128*, 2042.
(70) Baldus, M.; Petkova, A. T.; Herzfeld, J.; Griffin, R. G. *Mol. Phys.* **1998**, *95*, 1197.
(71) Bennett, A. E.; Rienstra, C. M.; Auger, M.; Lakshmi, K. V.; Griffin, R. G. *J. Chem. Phys.* **1995**, *103*, 6951.
(72) Gullion, T.; Schaefer, J. *J. Magn. Reson.* **1989**, *81*, 196.
(73) Oas, T. G.; Griffin, R. G.; Levitt, M. H. *J. Chem. Phys.* **1988**, *89*, 692.
(74) Gan, Z. H.; Grant, D. M. *Chem. Phys. Lett.* **1990**, *168*, 304.
(75) Kotecha, M.; Wickramasinghe, N. P.; Ishii, Y. *Magn. Reson. Chem.* **2007**, *45*, S221.
(76) Morcombe, C. R.; Zilm, K. W. *J. Magn. Reson.* **2003**, *162*, 479.
(77) Delaglio, F.; Grzesiek, S.; Vuister, G. W.; Zhu, G.; Pfeifer, J.; Bax, A. *J. Biomol. NMR* **1995**, *6*, 277.
(78) Keller, R. *The Computer Aided Resonance Assignment Tutorial*, 1st ed.; CANTINA Verlag: Germany, 2004.
(79) Rienstra, C. M.; Hohwy, M.; Mueller, L. J.; Jaroniec, C. P.; Reif, B.; Griffin, R. G. *J. Am. Chem. Soc.* **2002**, *124*, 11908.
(80) Allen, F. H.; Kennard, O.; Watson, D. G.; Brammer, L.; Orpen, A. G.; Taylor, R. *J. Chem. Soc., Perkin Trans. 2* **1987**, S1.
(81) Jaroniec, C. P.; Tounge, B. A.; Rienstra, C. M.; Herzfeld, J.; Griffin, R. G. *J. Magn. Reson.* **2000**, *146*, 132.
(82) Veshtort, M.; Griffin, R. G. *J. Magn. Reson.* **2006**, *178*, 248.
(83) Kurbanov, R.; Zinkevich, T.; Krushelnitsky, A. *J. Chem. Phys.* **2011**, 135.
(84) Wu, C. H.; Ramamoorthy, A.; Gierasch, L. M.; Opella, S. J. *J. Am. Chem. Soc.* **1995**, *117*, 6148.
(85) Wylie, B. J.; Franks, W. T.; Rienstra, C. M. *J. Phys. Chem. B* **2006**, *110*, 10926.
(86) Mollica, L.; Baias, M.; Lewandowski, J. R.; Wylie, B. J.; Sperling, L. J.; Rienstra, C. M.; Emsley, L.; Blackledge, M. *J. Phys. Chem. Lett.* **2012**, *3*, 3657.
(87) Gautier, A.; Mott, H. R.; Bostock, M. J.; Kirkpatrick, J. P.; Nietlispach, D. *Nat. Struct. Mol. Biol.* **2010**, *17*, 768.
(88) Shi, L.; Ahmed, M. A. M.; Zhang, W.; Whited, G.; Brown, L. S.; Ladizhansky, V. *J. Mol. Biol.* **2009**, *386*, 1078.
(89) Kim, J. M.; Booth, P. J.; Allen, S. J.; Khorana, H. G. *J. Mol. Biol.* **2001**, *308*, 409.
(90) Allen, S. J.; Kim, J. M.; Khorana, H. G.; Lu, H.; Booth, P. J. *J. Mol. Biol.* **2001**, *308*, 423.
(91) Rouhani, S.; Cartailler, J. P.; Facciotti, M. T.; Walian, P.; Needleman, R.; Lanyi, J. K.; Glaeser, R. M.; Luecke, H. *J. Mol. Biol.* **2001**, *313*, 615.
(92) Reuther, G.; Tan, K. T.; Vogel, A.; Nowak, C.; Arnold, K.; Kuhlmann, J.; Waldmann, H.; Huster, D. *J. Am. Chem. Soc.* **2006**, *128*, 13840.
(93) Scheidt, H. A.; Vogel, A.; Eckhoff, A.; Koenig, B. W.; Huster, D. *Eur. Biophys. J.* **2007**, *36*, 393.
(94) Kawamura, I.; Ohmine, M.; Tanabe, J.; Tuzi, S.; Saito, H.; Naito, A. *Biochim. Biophys. Acta* **2007**, *1768*, 3090.
(95) Altenbach, C.; Flitsch, S. L.; Khorana, H. G.; Hubbell, W. L. *Biochemistry* **1989**, *28*, 7806.
(96) Chen, D.; Wang, J. M.; Lanyi, J. K. *J. Mol. Biol.* **2007**, *366*, 790.
(97) Zhang, J.; Yamazaki, Y.; Hikake, M.; Murakami, M.; Ihara, K.; Kouyama, T. *Proteins* **2012**, *80*, 2384.
(98) Yamamoto, M.; Hayakawa, N.; Murakami, M.; Kouyama, T. *J. Mol. Biol.* **2009**, *393*, 559.
(99) Lewandowski, J. R.; Sein, J.; Blackledge, M.; Emsley, L. *J. Am. Chem. Soc.* **2010**, *132*, 1246.
(100) Lorieau, J. L.; Louis, J. M.; Bax, A. *J. Am. Chem. Soc.* **2011**, *133*, 14184.
(101) Lienin, S. F.; Bremi, T.; Brutscher, B.; Bruschweiler, R.; Ernst, R. R. *J. Am. Chem. Soc.* **1998**, *120*, 9870.
(102) Louet, M.; Karakas, E.; Perret, A.; Perahia, D.; Martinez, J.; Floquet, N. *FEBS Lett.* **2013**, *587*, 2656.